Blind comparison of saturation ratio profiles on large RC structures by means of NDT and SFE-Application to the VeRCoRs mock-up

Ritesh Gupta, Donatien Rossat, Xavier Dérobert, Julien Baroth, Matthieu Briffaut, Géraldine Villain, Frédéric Dufour

Blind comparison of saturation ratio profiles on large RC structures by means of NDT and SFE - Application to the VeRCoRS mock-up

Ritesh Gupta[a], Donatien Rossat[a,b], Xavier Dérobert[c], Julien Baroth[a,*], Matthieu Briffaut[d], Géraldine Villain[c], Frédéric Dufour[a]

[a] *Univ. Grenoble Alpes, CNRS, Grenoble INP, 3SR, 38000 Grenoble, France*
[b] *Electricité de France (EDF-DIPNN-DT), 69007 Lyon, France*
[c] *Univ Gustave Eiffel, Campus de Nantes, F-44344 Bouguenais, France*
[d] *Univ. Lille, CNRS, Centrale Lille, UMR 9013 - LaMcube - Laboratoire de Mécanique, Multiphysique, Multiéchelle, F-59000 Lille, France*

Abstract

The prediction of large concrete structures behaviour such as bridges, dams and nuclear containment buildings (NCB) is a vital issue regarding the evaluation of the durability, safety and effect on the surrounding environment. In this work, experimental and numerical estimations of the saturation ratio profiles in the VeRCoRs NCB mock-up structure are presented, and their blind comparison is discussed. Non-destructive testing (NDT) based capacitive measurements are processed to quantify the saturation ratio experimentally. Then, a weakly coupled thermo-hydric (TH) finite element model is presented within the serviceability state of VeRCoRs for the numerical counterpart. The uncertainty in the capacitive measurements and the constitutive parameters of the numerical model are highlighted as coming from the following three sources: (a) the natural randomness of the material properties and physical processes, (b) the limited

*Corresponding author
Email address: julien.baroth@3sr-grenoble.fr (Julien Baroth)

knowledge of some input parameters in the mathematical model either obtained experimentally at the specimen scale and (c) empirically derived in the exploitation of the physical process. The influence of the uncertainty in the saturation ratio estimations is presented by error bars experimentally and is addressed by a stochastic finite element (SFE) study in the numerical work. Accounting for uncertainties in NDT and SFE measurements, the mean values of saturation ratio (reported in %) profile are forecasted up to 40% and 34% respectively, with standard deviation for both in the range of 3.5-4.5% in magnitude.

Keywords: Concrete structures, Saturation ratio, Spatial distribution, Non-destructive capacitive measurements, Stochastic finite element analysis, Uncertainty quantification

---

1. Introduction

The prediction of the fluid-tightness of large concrete structures, especially those with a containment role such as Nuclear Containment Buildings (NCB), plays a crucial role in their serviceability and longevity and, most importantly, the safety of the surrounding environment. These large containment structures undergo complex physical processes (*e.g.*, concrete ageing) over their lifespan, and thus, the tightness evolves significantly during the lifetime of the structure. Therefore, it is necessary to account for uncertainties associated with numerical forecasts to quantify structural integrity and tightness risks and, therefore, provide decision aids for improving their maintenance. Apart from cracking at an early age at the outer structure surfaces, which is out of the scope of our contribution, concrete drying, a key durability indicator, must be carefully ad-

dressed. Concrete drying is a vital issue for the air-tightness of the structure as more connected porosity becomes available for gas molecule transfer upon drying. Besides, drying is of great importance for prestressed structures since the drying induced shrinkage accelerates the loss of prestressing effects.

To these ends, the VeRCoRs NCB mock-up has been chosen as an application case of a containment building in this work [1]. VeRCoRs is a $1:3$ structural scale mock-up of the double-wall containment enclosure constructed by EDF to experimentally analyse the time evolution of properties and behaviour of the containment enclosures under actual operating conditions. VeRCoRs (*Vérification Réaliste du Confinement des Réacteurs*) is a French acronym meaning 'realistic verification of the containment of the reactors'. The concrete drying behaviour investigation is taken as a proxy to address the aforementioned critical issues. The evolution of the saturation ratio is considered representative of the drying behaviour.

When considering the assessment of concrete structures on-site, non-destructive testing (NDT) techniques enable to completion of visual inspections and provide means to improve the reliability in the evaluation. Several NDTs have been developed for civil engineering applications, as being sensitive to different material properties like durability indicators and state parameters. Ultrasonic methods are applied for strength assessment through elastic modulus measurement and defect detection like the presence of air and crack [2, 3]. Also, the electromagnetic (EM) methods are proven sensitive to the water and ionic content [4, 5]. Therefore, they are helpful to measure the dielectric permittivity and electric

resistivity in concretes.

In recent years, non-destructive measurements have notably been provided by the ENDE (*Evaluation Non Destructive des Enceintes de confinement des centrales nucléaires*) research project, thanks to the PIA-RNSR French National Program, involving a wide range of non-destructive measurement techniques of several concrete properties (Young's modulus, porosity, permeability). The significant amount of measurement points provided by such techniques enables to perform much more consistent statistical inference.

The capacitive measurements are part of non-destructive testing (NDT) techniques useful for the evaluation of concrete structures [6, 7]. NDT techniques are not only significant for detecting peculiarities but also helpful in assessing concrete material properties and their spatial distribution and time evolution, like saturation ratio, during the diagnosis of civil engineering structures [5]. However, auscultation cannot only be based on NDTs as each one can be related to more than one durability indicator (*e.g.* saturation ratio, porosity and compressive strength). Hence, destructive tests (DT) are necessary to confirm and calibrate the results obtained by NDT auscultation [8].

Besides, numerical models are used to assess the pertinence of in-situ measurements and also predict the long term effect of ageing on the future behaviour of concrete [9]. Several numerical studies have been performed to assess the physical processes linked to large concrete containment structures in recent years. Several numerical models are available for purpose of covering the thermal [10] and hydric [11, 12, 13, 14] behavior of concrete using either a fully

coupled approaches [15, 16, 17, 18, 19] or chained calculation strategies [20, 21] also called weakly-coupled approaches. Based on our past experience [9, 22] and the results of the international blind benchmark [1], a weakly-coupled approach is chosen to offer an efficient optimum in this contribution. Thereby, drying is the only aging phenomenon taken into account in the present work. Notably, the hydric behaviour in this work refers to the time evolution of the moisture in the concrete and therefore can be interchangeably referred to as the hydraulic behaviour, a representative of the moisture transfer phenomenon.

In general, the model accuracy is dependent on the boundary conditions (BCs) and the uncertainties related to the concrete's properties' identification. These modelling approaches present the detailed deterministic description of the associated physical processes, accounting for the uncertainty in the input parameters and the uncertainty of the numerical forecast. For this, the general uncertainty Quantification (UQ) framework enables one to account for uncertainties associated with material properties, loads, or boundary conditions and quantify their influence on numerical predictions. It is generally achieved by using elements of probability theory, by modelling input parameters of a physical model as random variables and estimating statistical moments or probability density functions (PDFs) of the model response. In addition, simulation methods such as Monte-Carlo (MC) combined with surrogate modelling techniques are often used in this context [22]. The stochastic finite element (SFE) model forecast incorporates the law of large numbers and the central limit theorem to quantify the model response converging towards a mean magnitude.

In this work, independent experimental and numerical works towards estimating the saturation ratio profile in the VeRCoRs mock-up are presented and blindly compared. The capacitive measurements provide an extensive data set for the in-situ experimental measurements. A sparse Polynomial Chaos Expansion (PCE) surrogate of the thermo-hydric (TH) numerical model represents the stochastic saturation ratio.

The outline of the present work is briefed hereafter. First, the problem statement in the context of the VeRCoRs mock-up is presented. Second, the experimental work comprising the EM characterisation of the constituent concrete on the lab-scale specimens towards the calibration of the saturation ratio and in-situ capacitive measurements and their post-processing for the saturation ratio estimation is presented. Third, a numerical work comprising the finite element model representative of the VeRCoRs mock-up for a deterministic and stochastic estimation of the saturation ratio is presented. Lastly, the blind comparison of the saturation ratios estimations from two independent campaigns is presented alongside a discussion on agreement and difference.

2. Problem statement

This section presents the structural layout of the VeRCoRs mock-up, the concrete mix design composition and pressurization test loading history considered in this work. VeRCoRS is a non-nuclear containment mock-up; however, it is subjected to the same operating conditions as those familiar to a nuclear containment building. In addition, the mock-up is highly instrumented (*e.g.*

more than 700 sensors, 2 km of optical fibre and pendulums), providing real-time access to a database of physical measurements covering its entire operating life [1]. The concrete mix design of the VeRCoRs mockup enclosure is presented in Table 1.

Table 1: Concrete mix design of VeRCoRs mock-up, from [1]

Component		Quantity	Unit
Cement	CEM I 52.5	320	kg/m^3
Water		197.6	l/m^3
Sand	0/4 (GSM LGP1)	830	kg/m^3
Gravel	4/11 (GSM LGP1)	445	kg/m^3
	8/16 (Balloy, Seine-et-Marne)	550	kg/m^3
Admixture	Plasticising adjuvant	2.4	l/m^3
Density		2386	kg/m^3
w/c ratio	by weight	0.62	

Due to its reduced scale, the model ages more quickly than an actual enclosure. According to the preliminary studies of the project, a factor of 9 is retained to exploit the drying kinetics [1]. So a 60-year operating life for an actual enclosure would be represented by only 6.5 years at the 1:3 scale model. It allows simulating accelerated yet realistic drying behaviour during 60 years of operation.

The containment structure is made up of different structural components

of different dimensions and varying thicknesses, presented in Figure 1. Dimensional differences cause heterogeneous ageing in the structure as thin elements tend to age faster than thick elements. Moreover, it gives rise to differential deformations exposing the relatively thinner parts to a greater risk of cracking. Thus, wall region of 14.68m height, as seen from Figure 1b, is the focused area in the present work for the estimations of the saturation ratio profiles experimentally and numerically.

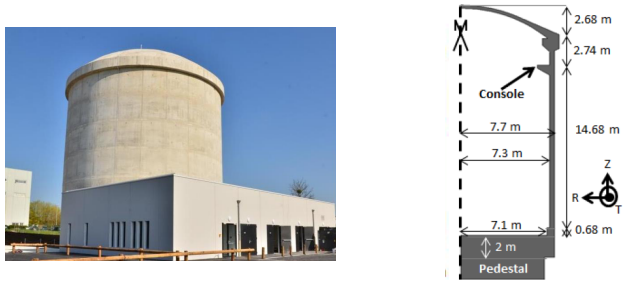

(a) (b)

Figure 1: General overview of the VeRCoRs mock-up, presenting (a) isometric view [23] (b) an asymmetric vertical sector of the inner wall of the mock-up, from [9]

A sequence of standardized pressurization tests verifies the serviceability of a full-scale NCB. First, tests are performed after prestressing the containment building and the commissioning of the reactor, named as pre-operational visit (VPO - *Visite pré-opérationnelle*). Next, the following test is performed three years after the first fuel loading named as additional visit (VC - *visite complémentaire*). Then every ten years, ten-yearly visits (VD - *visites décennales*). The scaled-down test timeline for the VeRCoRs mock-up is presented in Figure 2.

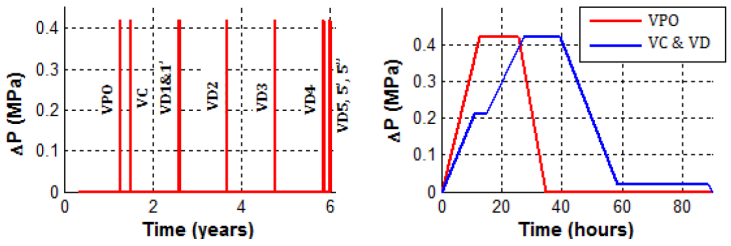

Figure 2: Pressurization/depressurisation tests timeline in VeRCoRs mock-up, from [9]

The pressure rise profiles differ from one enclosure to another; however, the principle remains the same [24, 25]. A gradual increase in the internal pressure until the target value of 5.2 bars absolute pressure is reached. The level is maintained at this sizing pressure for 24 hours, then progressive reduction of the overpressure until return to atmospheric pressure. The tests on the VeRCoRs mock-up enclosure are carried out under less aggressive conditions than for a full-scale model to avoid potential damage in the structure compromised in its future containment capacities [26]. Here, the dry air is inhibited, at a temperature of $20°C$, at a similar pressure difference between the inner and outer surface of the internal wall of 4.2 bars for the pressurization tests. In-situ NDT measurements on the containment structure during the pressurization tests provide extensive databases to assess its behaviour and estimate the relevant durability indicators. In the present work, the database recorded at the time instance of the test VD3 is presented hereafter to assess the saturation ratio.

3. Experimental saturation ratio estimation

The experimental campaign in the present work comprises of two parts. First, the electromagnetic characterisation of the VeRCoRs concrete is presented to define its complex permittivity characteristics. Subsequently, a calibration campaign on lab-scale samples with a similar mix design as of a vercors mock-up is presented to establish a relationship between concrete saturation ratio and relative permittivity measurements. Second, the calibrated relationship from the first part is used to characterise the on-site relative permittivity database extracted using electrode probes in the framework of the ENDE project as the on-site saturation ratio measurements. The description of the experimental work activities is presented hereafter.

3.1. Electromagnetic characterization of VeRCoRs concrete

The on-site capacitive technique is presented characterising the in situ dielectric media in the 30–35 MHz frequency band to measure the saturation ratio profile in different locations. A calibration methodology is necessary to evaluate the saturation ratio in various civil engineering structures [27]. Such methodology is based on the complex permittivity measurement on various dispersive concretes. The permittivity measurements are carried out by a cylindrical coaxial electromagnetic (EM) transition line. It allows the laboratory characterisation of the material specimens in a large ground penetration radar (GPR) frequency band (50– 1200 MHz approx.) such as asphalt or concrete mixes [28].

Thereby, large campaigns of EM characterisation of numerous concrete mixes

are processed to evaluate the influence of every composition parameter on the complex permittivity in the GPR frequency band, using a multi-linear polynomial model from [29]. In addition, several tests were performed studying the effect of water content, chloride content and carbonation on the complex permittivity of concrete mixes [30]. EM NDT is sensitive to the volumetric water content in the porous material. However, as structure engineers characterise moisture using saturation rate, EM laboratory measurements are transformed in saturation ratio values while considering the material bulk density. Therefore, in this work, the study on the saturation ratio parameter only is presented.

A methodology is developed to extrapolate EM cell measurements at low frequencies, using the four-parameter variant of Jonscher's model [27]. It enables to obtain dispersion curves of the complex permittivity for extensive frequency bands, including the frequency range of the capacitive technique (≈33 MHz).

In the ENDE project framework, nine concrete cores, each 70 mm long and 75 mm in diameter, are extracted from the concrete block prepared with the concrete mix design and at a timeline same as in VeRCoRs mock-up VD3 pressurisation test (see Figure 2). Eight cores are extracted from the center of the block and one from the surface. They are conditioned in the laboratory until the homogeneous saturation of about 100%, 70%, 50% and 10% are achieved [31]. The experimental campaign presents the macro-porosity measurements reported based on the amount of water present in the sample between dry and saturated states in normalised conditions [32].

The measured values of the concrete permittivities at different saturation

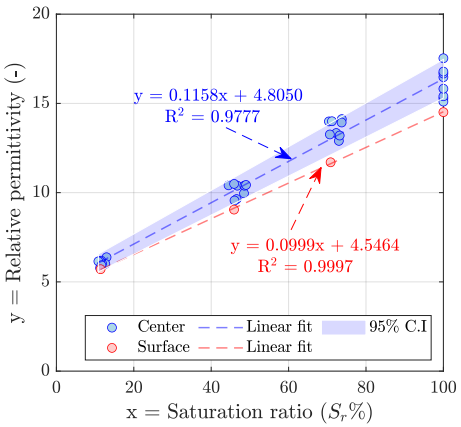

Figure 3: Permittivity (33 MHz) vs saturation ratio calibration curve for the VeRCoRs concrete

ratios, including a linear regression to present the overall trend, are presented in Figure 3. The regression obtained from the surface core is assumed to be a relatively better representative of capacitive measurements, which remain applicable to the first few centimetres of the VeRCoRs mock-up structure wall. A standard deviation of 0.37 is reported on the permittivity measurements of the center core is observed reported from the sample set of measurements. It induces a default uncertainty of $\pm 3.20\%$ on the saturation ratio magnitude obtained from a permittivity value using the calibration slope of the center cores. Besides, a porosity of 14.5% and a carbonation depth of about 3 mm is observed from the surface core. In contrast, the porosity measured from the average of the center cores is 15.8%. Higher relative permittivity measurements corresponding to the center cores can be inferred due to the relatively higher porosity.

3.2. Capacitive measurements on VeRCoRs mock-up

This section describes the principle of capacitive measurements conducted on VeRCoRs mock-up. The aim is to estimate the saturation ratio from the capacitive measurements while discussing the various sources of uncertainty. The principle of the technique used to investigate VeRCoRs mock-up is based on the measurement of a resonant frequency (around 33 MHz) of an oscillating electric circuit RIC (resistor/inductor/capacitor) type between electrodes placed on the testing material. The set of the electrodes and the medium forms the capacitor of the RIC circuit. It is dependent on the geometry of the electrodes and the relative permittivity of the medium [5].

The interest of a set of various electrodes is to be able to reach varying penetration depths and thus obtain information of a gradient along with depth [33]. Various electrode probes and geometrical parameters associated with operating frequency facilitate variation in investigation volumes corresponding to coupling volumes. The volume of material visible by the sensor influencing the measurement is termed the coupling volume. This technique is suitable for measuring the saturation ratio of porous materials, such as concrete. The system designed by the Technical and Scientific Network of the French Ministry of the Ecological Transition comprises a panel of several electrodes [6]. In this work, the electrodes PE (5x70 mm), ME (10x70 mm), M3E (15x70 mm) having coupling volumes of thicknesses about 7, 17 and 22mm respectively are used, as presented in Figure 4.

A calibration step is necessary to link the resonant frequency to a permit-

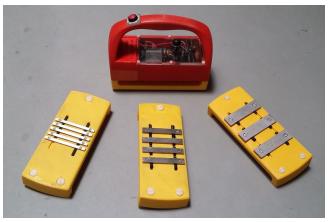

Figure 4: Capacitive measurements electrodes PE, ME and M3E as seen from left to right

tivity value, considering the medium as homogeneous and semi-infinite. Several known materials are used as reference whose permittivities are measured in an EM cell. These materials include PVC, Teflon, marble, granite, limestone and eccostock, a rigid polyurethane foam of high permittivity [28]. Moreover, the interference effects of the external environment and the capacitive system is removed by a complementary measurement in the air, subtracted to the surveyed medium measurement. Thus, the variation of resonant frequency is linked to permittivity through this calibration step [27].

Notably, the relative permittivity measurements based on the capacitive method have several potential sources of uncertainty. These sources are briefly discussed below.

(a) Concrete characteristics: The EM nature of the aggregates, the type of cement, and the structure's porosity are influential parameters. Also, the porosity state can affect the relation between permittivity and water content from one concrete to another.

(b) Geometrical/structural characteristics: The curvature of the concrete structure, surface roughness, and the interface's quality interfere with the quality of the relative permittivity measurements. Also, the steel reinforcement in

the coupling volume of the electrodes is a critical source of measurement uncertainty due to the different EM characteristics of the reinforcement than the surrounding concrete. Lastly, the size of the coupling volume, smaller than the elementary representative volume of a mix like concrete, leads to the potential uncertainty in the measurements.

(c) Environmental characteristics: The permittivity of concrete roughly increases linearly with temperature in the range ($5 - 45°$C) with a relative slope of about $0.2 - 0.3\%/°C$ [34]. Also, the permittivity increases linearly with the volumetric water content with a relative slope of about $0.65 - 0.75\%/\%_{wc}$ [27]. Nonetheless, subtracting two successive measurements, one in the air and another in the concrete, removes significant environmental uncertainties.

(d) Data acquisition characteristics: The operator influence, the measurement system pressure on concrete and the repeatability of measurements are potential sources of uncertainty. Also, the regression selection on the calibration master curve to correlate EM measurements to the relative permittivity brings potential uncertainty. The trend is linear in the low permittivity range and exponential for high permittivities [33].

In the ANR-SENSO project framework, several NDT experiments are performed on controlled homogeneous concrete slabs [8]. These tests are based on many different methods such as ultrasonics, radar, capacitive and resistivity. Their sensitivity and variability are used to evaluate several indicators of concrete condition, such as porosity, Young's modulus, compressive strength at 28 days and water content. Then, an extensive database of about 200,000 data

points is provided and studied through statistical data analysis and data fusion. Relationships between NDT measurements and indicators are determined, and the variability analysis is presented (refer to Appendix A).

Three vertical lines were tested in the framework of the ENDE project over the entire height of the structure on the same meshes. The capacitive measurements at vertical lines V1, V2 and V3, are presented in Figure 5. The vertical lines V1 and V2 are tested at 12 measurement points over the height of about 13 m. The vertical line V3 is tested with 33 measurement points at the height of about 15 m.

The general methodology of investigation while using a GPR consists of locating the rebars. Once localized, five capacitive measurements are performed in the neighbourhood of the center of the chosen meshes. The averaged value, subtracted from the air measurement, is used to estimate the permittivity of the local area, and the standard deviation of the five measurements is recorded. The horizontal error bars in the relative permittivity measurement correspond to the standard deviation of the five measurements points in a chosen mesh.

The saturation ratios corresponding to the capacitive measurements are evaluated following the surface core regression (see Figure 3) and are presented in Figure 5. The horizontal error bars in the saturation ratio estimations correspond to the standard deviation corresponding to the uncertainty coming from the two following sources. The first corresponds to the local standard deviation in the relative permittivity at one point. The second one corresponds to the 3.20% (in magnitude) standard deviation obtained from the regression line of

the multiple measurements of the center core.

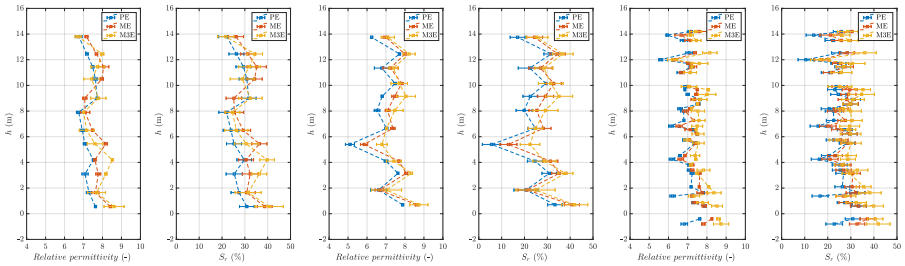

(a) Vertical line V1 (b) Vertical line V2 (c) Vertical line V3

Figure 5: Capacitive measurements and subsequently exploited saturation ratio (S_r) profiles on the three vertical lines in the VeRCoRS mock-up outer surface of the inner wall

Here, a specific trend on the capacitive measurements is not visible to explicitly explore the uncertainties in the measurements with the type of electrode used. Nonetheless, a general permittivity gradient with wall depth is observed, attributed to natural drying. Similarly, a general trend of saturation ratio decrease vs height is observed. It could be due to the aerial thermal gradient remaining inside the structure, accelerating the drying of the concrete structure with increasing height. The oscillating experimental measurements over the wall height are attributed to the ambient temperature on the concrete pouring day and the concreting schedule (mainly three batches per lift and time between lifts). These variations affect the 28-days compressive strength and Young's modulus, subsequently leading to varying relative permittivity.

Overall, the experimental database and the estimation of the saturation ratios based on the capacities measurements enable a good understanding of the instantaneous drying behaviour of the VeRCoRs mock-up. The detailed explo-

ration of the hydric response over the structure's lifetime calls for a numerical finite element model of the VeRCoRs mock-up, presented in the following section. The uncertainty in the model constituent parameters is addressed to estimate the numerical saturation ratio corresponding to the pressurisation test VD3 for its comparison with the in-situ measurements.

4. Numerical saturation ratio estimations

This section presents the numerical model framework of the drying phenomenon in the VeRCoRs mock-up. A weakly coupled thermo-hydric modelling strategy is used. The reference inner NCB temperature and external ambient temperatures for the thermal exchange are 35°C and 20°C respectively. The comparatively higher temperature inside results in a lower relative humidity in the concrete, losing the symmetry through the wall thickness and thus accelerates the drying of concrete. The composition of thermal and hydric phases is presented hereafter.

4.1. TH constitutive model

Thermal phase (T)

The temperature field is calculated using the classic heat equation, with no source term and assuming constant thermal diffusivity.

$$\rho_c C_c^p \frac{\partial T}{\partial t} - \nabla \cdot (\lambda_{hc} \nabla T) = 0 \tag{1}$$

Here, ρ_c is the mass density (2368 kg/m^3), C_c^p is the thermal capacity (880 $J/kg/°\mathrm{K}$) and λ_{hc} is long term thermal conductivity (2.5 $J/s/m/°\mathrm{K}$) of concrete.

Limiting conditions of the linear Neumann type are retained via the definition of convective fluxes following Newton's law for the internal and external surfaces of the model, presented in Equation 2.

$$-\vec{q}.\vec{n} = h_{eq,th}(T - T_{ext}) \tag{2}$$

Here, $h_{eq,th}$ is the thermal exchange coefficient (10 $J/m^2/s/°\mathrm{K}$) of concrete.

Hydric phase (H)

In this phase, the evolution of free water content, C_{fw}, (%) in the concrete's volume when exposed to a hydric flow, is presented. Water movement within the concrete's connected capillary pores is governed by complex, micro-structural, simultaneous and multiphasic processes such as diffusion, evaporation and condensation [35], [36]. The drying kinetics in the concrete is highly dependent on the relative humidity (RH) within its porosity. Thereby, for a high RH ($> 50\%$), the liquid water diffusivity due to water concentration and saturation rate gradients in the concrete volume mainly control the drying kinetics. In contrast, for a low RH ($< 20\%$), the vapour diffusivity controls the drying kinetics [37]. In the framework of the present work, the drying problem is reduced to the mass conservation of liquid water only.

$$\frac{\partial C_{fw}}{\partial t} = \nabla\cdot\left(D(C_{fw}, T)\nabla C_{fw}\right) \tag{3}$$

Here, the diffusion coefficient 'D' (m^2/s) is computed using a phenomenological approach: a coupled expression from Mensi [11] and Granger [14] models. It is thermo-activated according to the Arrhenius law [12]:

$$D(C_{fw}, T) = Ae^{BC_{fw}} \frac{T}{T^w_{ref}} e^{\left[-\frac{E^w_a}{R}\left(\frac{1}{T}-\frac{1}{T^w_{ref}}\right)\right]} \tag{4}$$

Here, A (3.18 $\mu m^2/s$) and B (0.057) are the parameters obtained from the fitting with the experimental results on concrete mass loss with time for heating at 20°C temperature and 50% RH, E^w_a is the activation energy (39000 J/mol) for drying, T^w_{ref} (15°C) is the reference temperature for thermo-activation of the water diffusion and 'R' is the ideal gas constant.

The hydric flow in the boundaries is due to relative humidity (RH) between the concrete's exposed edges and the external environment. The presented drying model uses the water content as the unknown parameter, while the boundary behaviour is expressed by RH. Thus, the two parameters are related through the sorption-desorption curve. However, the evolution is different because of the different kinetics inducing water loss and gain, meaning that the diffusivity factor is not the same during drying and wetting.

In this work, it is assumed that only the kinetics of drying is affected for the thermal loads considered during the operational phase. It remains valid during the period over which the concrete's RH is higher than the ambient air. Also, the VeRCoRs mock-up is a doubled wall structure and therefore, the outer face of the TH model of inner-wall is protected from the rain. Therefore, the mock-up inner wall boundaries are temperate with no season at a very high

RH in the ambient air. Hence, only the desorption curve is taken as sufficient representative of the continuous drying. The water content is related to RH via the desorption model [9, 38, 39]:

$$C_{fw} = C_{fw,0}\left(1 + \left(a \ln\left(\frac{1}{RH}\right)\right)^{\frac{1}{1-b}}\right)^{-b} \tag{5}$$

Here, $C_{fw,0}$ is the water content at $RH = 100\%$ considered representative of the one at the end of the hydration process under endogenous conditions. The parameters $a = 7.60$ and $b = 0.33$ are the empirical coefficients to represent the numerical desorption isotherm following the experimental measurement of the desorption and the concrete mass loss evolution with time at temperature of 20°C and RH of 50% [26]. Notably, during the pressurization tests, the temperature on the internal face of the inner wall rises to about 35°C. In contrast, the outer face temperatures remain at the NTP conditions varying with different seasons. Therefore, a compromise is made to simplify the desorption curve for the available limited experimental data at 20°C reference temperature, representing the drying behaviour.

Subsequently, the saturation ratio, S_r (in %), evolving in space, $\mathbf{x}$ and time, t is expressed as the portion of the capillary voids occupied by water, presented in Equation 6.

$$S_r(\mathbf{x}, t) = \frac{1}{\phi_V} C_{fw}(\mathbf{x}, t) \tag{6}$$

Here, $\phi_V = 14.6\%$ [1] is the connected capillary voids volume at the end of hydration.

Following the work of [9], a linear flux of RH is adopted to define the boundary conditions at the internal and external surfaces of the model, presented in Equation 7. It turns into a nonlinear Neumann type boundary condition as the RH is a nonlinear function of the water content.

$$-\vec{q}.\vec{n} = h_{eq,w}(RH - RH_{ext}) \tag{7}$$

Here, $h_{eq,w}$ is the hydric exchange coefficient (4.13 nm/s) which depends on the surface state, the ambient temperature and the vapour pressure, and RH_{ext} is the relative humidity of the external environment.

4.2. TH structural model

The model constitution is implemented on a 2D axisymmetric vertical section of the VeRCoRs mock-up in the finite element framework of *Code_Aster* solver [40]. The finite element (FE) mesh is made of linear quadrangular elements QUAD4, presented in Figure 6. Triangular linear elements TRIA3 are used to provide junctions in geometrically singular areas such as the dome-wall junction. The typical size of the FEs is 4 cm, and the mesh comprises 7629 nodes.

The in-situ measurements of the ambient air temperature of the internal enclosure and the space between enclosures are available only at three locations, one located at the level of the gusset ($z_1 = 4.0$ m), and the other two at different altitudes of the wall ($z_2 = 11.8$ m and $z_3 = 19.5$ m) [1]. Therefore, for the temperature fields on internal/external surfaces, a piece-wise linear distribution is constructed by dividing the height of the enclosure (noted Ω) into two zones,

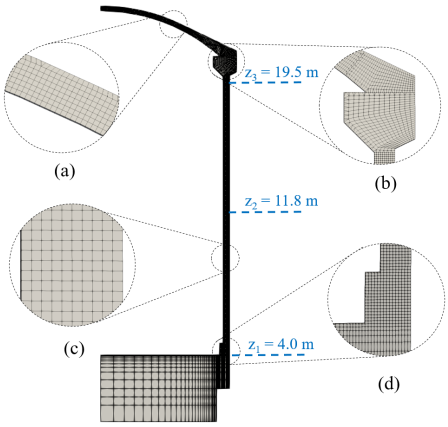

Figure 6: Mesh design of the VeRCoRs mock-up axisymmetric model representing different zones: (a) Dome, (b) dome-wall junction, (c) wall, and (d) gusset

394 presented in Equation 8.

$$\Omega_{ij} = \Omega \cap \{(x, y, z) \in \Omega \mid z_i \leq z \leq z_j\},\ \forall i, j \in \{1, 2, 3\},\ i < j \tag{8}$$

395 Noting T_i^{int}, T_i^{ext} as the air temperature measured at altitude z_i of internal
396 and external surfaces respectively, the corresponding air temperature field T_{air}^{int}
397 (resp. T_{air}^{ext}) is then constructed:

$$T_{air}^{\star}(z,t) = \left(\frac{z_j - z}{z_j - z_i}\right) T_i(t) + \left(\frac{z - z_i}{z_j - z_i}\right) T_j(t) \text{ for } z \in [z_i, z_j],\ \forall i, j \in \{1, 2, 3\},\ i < j \tag{9}$$

398 where $\star \in \{int, ext\}$.

399 The subsequent time evolution of the air temperatures in the inner and
400 outer surfaces are presented in Figure 7. The temperature variations before the
401 heating (at around 1.6 years) are observed similarly in the inner/outer faces.

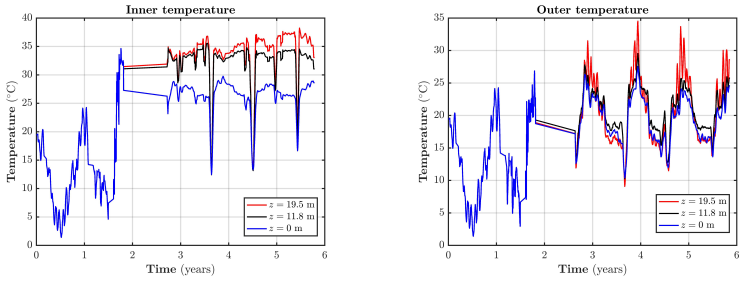

(a) (b)

Figure 7: Time evolution of the ambient air temperature measured in the the lifetime of the VeRCoRs mock-up

Afterwards, the temperature of inner air is raised and kept approximately at 35°C. However, warmer air is observed in the top region due to the internal air temperature stratification. Subsequently, a higher ambient temperature near the dome and a lower near the gusset are recorded. The heating is stopped during simulated unit outages momentarily before the internal pressure is applied in the framework of pressurisation tests. The temperature is kept approximately at 15°C as seen from the peaks on the inner air temperature profiles. The external temperature profiles are seasonal variations controlled and delayed by conduction ensured by the outer wall and its inertia. Also, fewer variations over the wall height in comparison to the inner wall are observed. Notably, the field data is missing between 1.9 to 2.7 years.

The temperature field at the times instances of the pressurisation tests is presented in Figure 8. In addition, the inner and outer surfaces temperature difference and its evolution during the pressurisation test instances are presented.

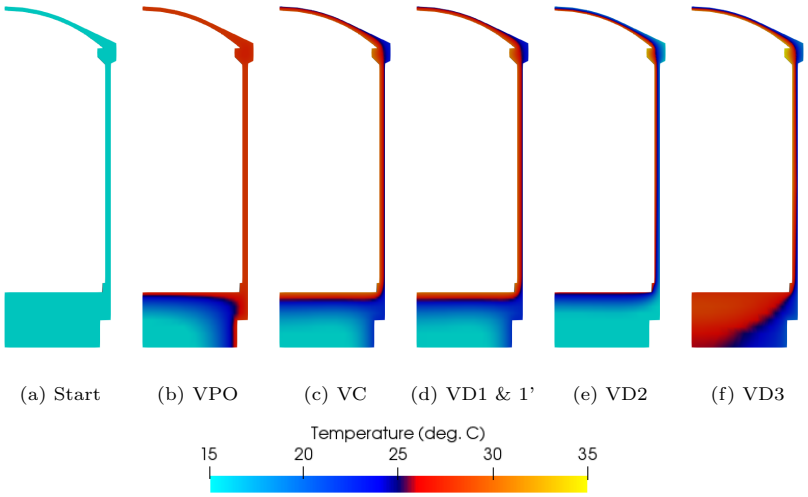

Figure 8: Time evolution of the temperature field in the VeRCoRs mock-up axisymmetric model at different pressurization/depressurisation test instances

The temperature field at the pressurization test instance VD3 is further explored for its intricacy in different regions of the structure as presented in Figure 9. The temperature in the internal and external wall faces in the wall region is about 32 °C and 23 °C respectively. The effect of wall thickness variation from 40 cm to 60 cm at the gusset level for the temperature evolution is observed. Besides the 40cm wall region is the area of interest in this work, the TH model is simulated for the mesh without the dome region of the structure aimed at computational time reduction. We observe the same temperature profile in the wall and gusset regions. Besides the faster computation, removing the dome region also simplifies the mesh design comprising only quadrangular elements QUAD4. Furthermore, it removes the potential issue of the singularity

428 at the junction for different mesh sizes design.

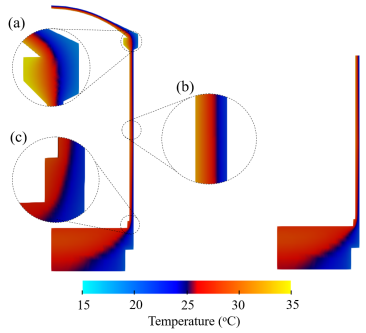

Figure 9: Temperature field at time instance of test VD3 for the full 2D mesh (left) and the mesh without dome region (right), also presenting the details of (a) dome, (b) wall and (c) gusset regions

429 Further, for the model hydric phase input, the in-situ measurements of the
430 relative humidity (RH_{air}) of the air in the enclosure are not available. Therefore,
431 the correlation between the RH_{air} and the temperature of the ambient air (T_{air})
432 is expressed by the use of Magnus law (referenced in Bouhjiti et al. [9]), is
433 presented in Equation 10.

$$RH_{air} = 163.61 \frac{r}{r + 0.62} \quad e^{-\frac{17.5043 \quad T_{air}}{241.2 + T_{air}}} \tag{10}$$

434 Here, '$r = 7$g/kg' is the air-water mixing ratio.

435 The *Code_Aster* FE code allows to create a user-defined non-linear flux only
436 in space or in time but not both. Therefore, given this hypothesis, a spatial TH
437 boundaries variation is considered to predict the drying behaviour while using
438 a time average of the temperature (and thus RH) two successive drying time
439 instances.

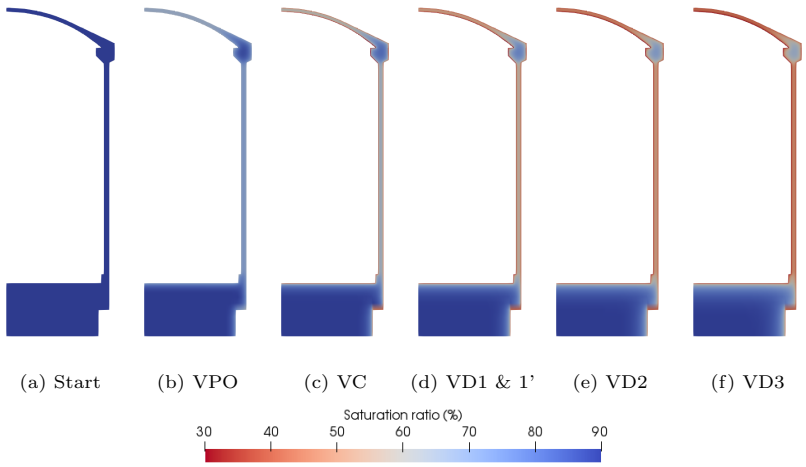

Figure 10: Time evolution of the satutation ratio field in the VeRCoRs mock-up axisymmetric model at different pressurization/depressurisation test instances

The time evolution of the degree of water saturation field is given in Figure 10. As applicable, an adaptive time scheme linked to the characteristic time of the diffusion equation solution is implemented between successive time instances. Subsequently, a total of 153 calculation instances for the drying of the model over 5.5 years are recorded. The start of drying is considered at 6^{th} month after the concrete pouring, as representative of the completion of the concrete hydration process and early age behaviour. Notably, the $S_r = 90\%$ is thus computed at the start of the drying process, based on Equation 6.

Similar to the thermal phase output, the saturation ratio (S_r) fields are presented in Figure 10 at the time instances of the pressurisation tests. Again, a significant drop is observed in the first two years and relatively consistent for the later stages when the inner temperature was raised to about 35°C.

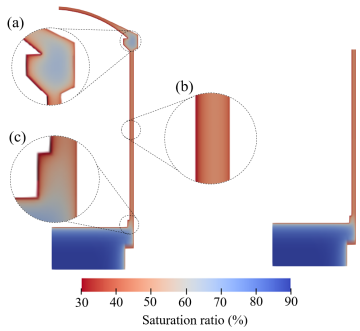

Figure 11: Saturation ratio field at time instance of test VD3 for the full 2D mesh (left) and the mesh without dome region (right), also presenting the details of (a) dome, (b) wall and (c) gusset regions

The detail of the saturation field at different zones of VeRCoRs mock-up at $t = 4.7$ years are presented in Figure 11. After 4.7 years of drying, the degree of saturation at the heart of the current zone is on average equal to 50%. The faster drying kinetics of the dome induces a degree of saturation of 45% at the core. Because of its thickness, the wall remains more saturated, with a core saturation of about 75%. The degree of saturation at the heart of the gusset is about 60%. Nearby the gusset step, a saturation of the order of 50% is observed due to a thermal bridge effect. Also, the computed saturation ratio field is observed the same for computations on a full 2D mesh and without dome mesh. Thereby, all computations and analyses presented here onward are performed on 2D mesh without dome region.

Finally, the mesh design along the wall height is optimised for coherent S_r estimations with the least computational time of T and H phases simulations. The time optimised mesh element distribution along with the wall thickness is

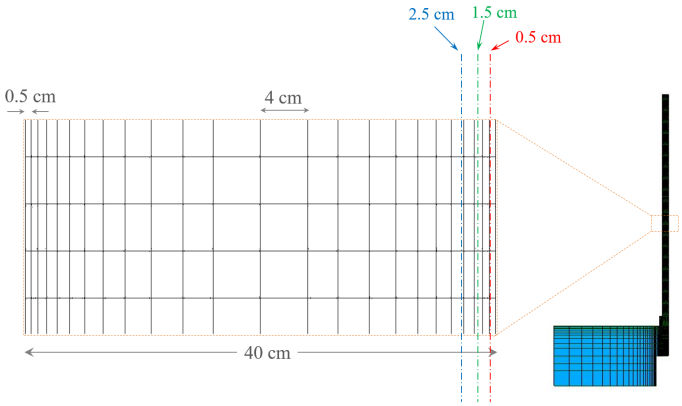

Figure 12: Optimised mesh configuration along wall and three depth levels selected for the degree of saturation computations and comparison with the experimental measurements at the zones of respective depth levels

presented in Figure 12. The elements are distributed with varying thicknesses from 0.5 cm at the wall edges to 4 cm in the wall center.

The time evolution of the saturation ratio from the TH model is explored at three vertical lines at depth levels of 0.5cm, 1.5cm and 2.5cm, representing the corresponding depths of in-situ electrodes PE, ME and M3E, respectively. Furthermore, the saturation ratio calculated from the TH model at the test VD3 is compared with the saturation ratio estimated from the capacitive measurements. Notably, the estimations from the experimental and numerical campaigns are independent of each other. Therefore, the blind comparison aims to understand the difference in the saturation ratio estimation from the two campaigns and discuss the potential sources of the difference and their associated impact with the engineering application point of view.

5. Blind comparison of experimental and numerical estimations

The drying phenomenon in the wall region is investigated under deterministic and probabilistic frameworks. It is aimed to estimate the numerical saturation ratio profile and compare it with the experimental counterpart.

5.1. Deterministic numerical vs mean experimental comparison

The TH model is solved deterministically, with the magnitudes of the parameters reported in the TH model constitution (see section 4.1). The experimental measurements of the saturation ratio are the outcome of the capacitive measurements carried out with three types of electrodes, at variable measurement thicknesses, from 5 mm to 3 cm. The comparison of the calculated saturation ratios from the TH model at the time instance of the pressurisation test VD3 with the linear regression plot of the mean magnitude of the saturation ratio from all the capacitive measurements along with wall height for the respective vertical lines is presented in Figure 13.

The calculated degree of saturation does not vary significantly with altitude as spatially varying material properties and thus spatially varying diffusivity are not considered in the TH model. On average, the degree of saturation computed from the TH model on the external face is slightly lower ($\approx 1\%$ at 0.5cm depth to $\approx 1.5\%$ at 2.5cm depth) in the top region of the wall than at the level of the gusset. A similar qualitative mean trend is observed in the experimental measurements. The mean trend given by the capacitive measurements is determined via a linear regression by ordinary least squares with weighting

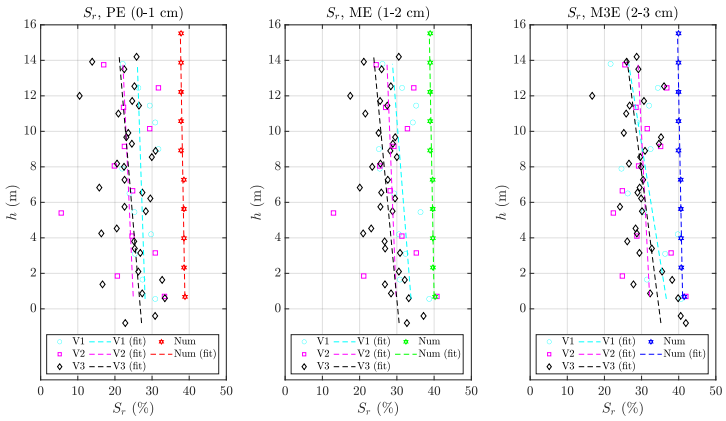

Figure 13: Saturation ratio profile at three depth levels from the deterministic solution of the TH model at the instance of the VD3 pressurisation test and comparison with the mean of the experimental measurements

by the inverse of the measurement uncertainties. In general, the slope of the mean experimental trend is observed higher than the numerical mean trend. Amongst the three vertical lines, line V2 presents the slightest varying slope of mean saturation ratio ($\approx 0.15\%$/m) along with the wall height for all three depth levels. For vertical line V1, the slope of mean S_r increases with increasing depth level starting from $\approx 0.20\%$/m at <5mm depth, increasing to 0.35%/m at 1-2cm depth and lastly further increasing to 0.70%/m at 2-3cm depth level. For vertical line V3, the number of measurements points are higher than the other two. However, the slope is intermediate between V1 and V2 measurements and is nearly consistent ($\approx 0.50\%$/m). The coherence of experimental measurements along three vertical lines is highest with M3E type electrode measurements at the same depth level. In contrast, the mean trends from PE and ME electrodes are comparatively scattered.

Overall, the numerically estimated saturation ratios are 5-10% in magnitude higher than the mean experimental counterpart. Comparatively, the experimental measurements approach closer to the numerical estimations with increasing depth level. The comparative saturation ratio increase with depth level is observed higher for the capacitive measurements than in the numerical model. It is arguably due to a higher magnitude of the hydric exchange coefficient ($h_{eq,w}$) in the model (than in reality), resulting in the faster inward movement of the drying front and hence keeping the rate of saturation ratio increase with depth low. However, the higher RH at the boundaries provides compensation for the faster rate of dry front movement. The incumbent reasons for the difference are the uncertainties in the experimental measurements and approximations in the numerical estimations. From an application point of view, this difference presents essential information on the critical parameters necessary to identify their experimental measurements. It also necessarily points out the consequences of the numerical computations approximation.

For example, the RH is averaged between two successive time instances in numerical computations, assuming the drying kinetics are insignificantly influenced by the varying temperature over time. However, the experimental measurements are carried out at a controlled room temperature ($\approx$ 20-25 °C) at a specific time instance. So, a potential difference between the ambient air temperature between experimental and numerical estimations subsequently leads to the different RH and thus different S_r. However, in this work, the calibration curve is relevant, assuming that the difference between the lab-scale specimen

and in-situ capacitive measurements is not significant.

The higher mean magnitude in the numerical estimations can be attributed to the initial water content taken, assuming an initial saturation ratio of 90% at the end of the early age of the concrete. If there is a lower bound uncertainly of 10% in the initial saturation ratio (i.e. if the initial water content occupies 80% porosity), then subsequent saturation ratio magnitude at the timeline of test VD3 drops by 3.9% on an average.

Nonetheless, comparing the numerical model response obtained by a single set of parameters provides limited and less reliable information. The uncertainty in the input parameters and the resulting consequence on saturation ratio is crucial to take into account for the correct and reliable predictions from the TH model. For this, a stochastic numerical study on the TH model is presented hereafter.

5.2. Stochastic numerical vs experimental comparison

This section presents a stochastic study on the TH model to address the uncertainty in the input parameters (in terms of the range of their magnitudes) and their subsequent influence in estimating the saturation ratio profile. First, a preliminary sensitivity analysis is presented to establish a set of the most influential parameters on the model response with the least possible computation cost. Subsequently, an extensive probabilistic sensitivity analysis is presented using the polynomial chaos expansion (PCE) based surrogate model for the cost-effective large computations of the TH model. Lastly, the stochastic model output is compared with the experimental counterpart alongside a discussion

on the blind comparison.

Table 2: List of parameters used for the deterministic computation at mean values and characteristic of the uniform distribution retained for the stochastic analysis

Input parameters	Mean magnitude	Uniform distribution bounds		Reference
		Minimum	Maximum	
Thermal (T)				
λ_{hc} $(kJ/h/m/°C)$	4.18	2.51	5.85	[26]
$h_{eq,th}$ $(kJ/h/m/°C)$	36.0	21.6	50.4	[41]
Hydric (H)				
$S_{r,0}$ (%)	90	80	100	[1]
ϕ_V (l/m^3)	146.0	138.7	153.3	[1]
$A \times 10^{-12}$ (m^2/s)	3.18	2.54	3.82	
$B \times 10^{-2}$	5.7	4.6	6.8	
$h_{eq,w}$ (nm/s)	4.13	2.68	5.58	
E_a^w (kJ/mol)	39.00	29.25	48.75	[26]

A set of 8 input parameters from thermal (T) and hydric (H) phases is established, presented in Table 2, to explore the influence of each one on saturation ratio computations. Two parameters (λ_{hc} and $h_{eq,th}$) are selected from the thermal phase where the first one takes into account the uncertainty in the thermal diffusivity while the second one associates the uncertainty in the thermal boundary condition. Notably, the thermal capacity parameter (C_c^p) is

influential for the thermal phase behaviour only at an early age. Hence, it is not taken into account for the sensitivity study of the long-term behaviour [26].

Similarly, six parameters from the hydric phase constitution are selected for the sensitivity analysis. The initial saturation ratio ($S_{r,0}$) parameter is taken as an indirect representative of the initial water content ($C_{fw,0}$) to keep $S_{r,0} \leq 1$ in all the possible input set of the parameters. The uncertainty in the $C_{fw,0}$ measurement is based on the observed difference between thermogravimetric analysis estimation [1] and the one based on Powers and Brownyard model [42]. The porosity measurements and the associated uncertainty are selected based on the reported results in [1]. The mean magnitudes of the parameters E_a^w and $h_{eq,w}$ are taken from previous studies [11, 14, 13, 12]. The parameters A and B are selected through iterative adjustments of the selected couple of values (A, B), for which the sum of squared residuals is the least in the experimental mass loss curve [26]. Further, The mean magnitudes of the parameters A, B and $h_{eq,w}$ are updated based on the statistical treatment of the hydric phase by Bayesian calibration strategy. Lastly, the relative humidity of the ambient air, RH_{air}, (Equation 10) is estimated based on the temperature measurements from Equation 9 interpolated over the wall height. Relative humidity estimations are observed insensitive to the uncertainty of $\pm 15\%$ in the magnitude of the parameter 'r', estimated in the field [1]. Therefore, the parameter 'r' and subsequently, the RH_{air} is not considered for the sensitivity analysis.

Here, for the sensitivity analysis, the ANOVA (ANalysis Of VAriance) framework is adopted, where a parameter is said to be influent (in first-order) if its

variations sensibly contribute to the response variance. Sobol' indices [43] sensitivity method belongs to this category. However, it requires many computations (of order 10^6 or more) for correct estimations. Therefore, a priori, one factor at a time (OFAT) type sensitivity analysis methods are explored to establish a preliminary understanding of the phenomena with a reasonable computational cost. The sensitivity analysis module of UQLab [44] presents two OFAT methods, namely perturbation method and Cotter's method [45], termed as linearisation based methods. Furthermore, the Morris method [46] is used for the preliminary understanding of the sensitivity of the input variables. The Morris method is closely similar to Cotter's method but provides a better exhaustive cover to the entire input space.

In this work, first, 1D TH model computations are performed for the sensitivity analysis based on perturbation Cotter and Morris methods. The number of model evaluations for Morris methods is chosen to be 600, owing to the low computation time for 1D calculations. Furthermore, the similarity in input parameters ranking for sensitivity is observed between all three methods. However, the perturbation method provided minor clear information, and the Morris method requires many model computations (of order $> 10^4$) for accurate computations. Subsequently, Cotter's method is chosen for preliminary sensitivity analysis with 'N = 8' input parameters and presented in detail hereafter.

The Cotter's method sensitivity analysis for the parameters listed in Table 2 is carried out on the optimised model 2D mesh for 'S_r' computations. Cotter's method is a low-cost and straightforward method for ranking input parameters

as the Cotter indices. It is based on the assumption that the model is linear or linearised around a central value. However, the presented TH model exhibits a non-linear behaviour. Therefore, the linearisation assumption oversimplifies the model response yet is relevant for the preliminary understanding of the sensitivity of the constituent parameters. Besides, it can be applied regardless of dependence between the input variables [44]. A brief description of Cotter's method formulation is presented in Appendix B.1.

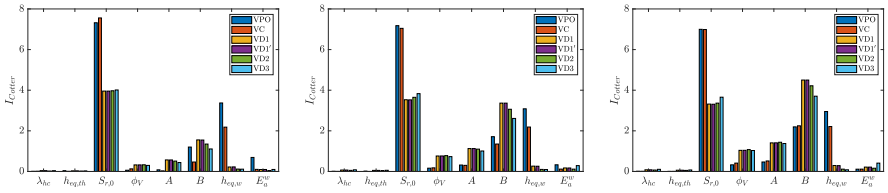

(a) at 0.5cm depth (b) at 1.5cm depth (c) at 2.5cm depth

Figure 14: Cotter's method [45] based Sensitivity analysis of the degree of saturation profile from 2D TH computations on the optimised mesh at mid-wall height for three different depth levels

The timeline of the pressurisation tests (indicated in Figure 2) is used to compute the Cotter indices at the equivalent six test instances, presented in Figure 14. The indices reflect the negligible effect of variability of the thermal phase parameters (λ_{hc} and $h_{eq,th}$) on the saturation ratio profile computation for all six test instances. Similarly, in the hydric phase, the variation in the activation energy for drying (E_a^w) also negligibly affects the saturation ratio computation. At 0.5cm depth, the initial saturation ratio ($S_{r,0}$) is observed most influential in the first two test instances and constant for the later four

test instances. A correlation between the evolution of the saturation ratio field presented in Figure 10 and the Cotter indices for $S_{r,0}$ presents direct relevance where S_r is higher (in the range 63-67%) for the first two tests and lower (in the range 38-43%) for the last four tests. A similar trend in Cotter indices is observed for the available porosity ϕ_V, however, lower in the index magnitude. Further, the parameters A and B, associated with the diffusivity coefficient, present the opposite trend, being lower for the first two instances and higher for the latest four instances. The trend presents an indirect correlation between the significance of the saturation ratio on the diffusion phenomenon.

A similar trend is observed at 1.5 and 2.5cm depth levels for the parameter ranking based on Cotter indices. The pore network parameters ($s_{r,0}$ and ϕ_V) present a slight decrease in the sensitivity with increasing depth. It infers the relatively higher significance of boundary conditions on the hydric exchange. The parameters A and B, related to the diffusion coefficient, present an increasing sensitivity trend with depth and thus indicate faster drying kinetics near the boundary. The same observation can be accessed from the increasing sensitivity of the hydric exchange coefficient ($h_{eq,w}$) with depth.

Now, having established a preliminary understanding of the sensitivity of the input parameters, the further stochastic model analysis requires a large number of computations (e.g. using the MC simulation method). The computational time is $\approx$ 3 mins for one call to the TH model. Hence, a large number of model computations are unaffordable yet necessary. Meta-modelling provides an optimum between the two factors (cost and necessity) for the quality of the

computations by substituting the expensive-to-evaluate computational models with inexpensive-to-evaluate surrogates. In this work, polynomial chaos expansions (PCE) surrogate models are used to approximate the response of the TH FE model. The PCE is a powerful meta-modelling technique aiming at providing a functional approximation of a computational model through its spectral representation on a suitably built basis of orthonormal polynomials [22]. A brief description related to the PCE surrogate model deployed in this work is presented in Appendix B.2.

The PCE module of UQLab is used to define the sparse PCE surrogate model configured with the least angle regression (LARS) [47]. The five most sensitive parameters ($S_{r,0}, \phi_V, A, B, h_{eq,w}$) observed from the Cotter indices (see Figure 14) at all three depth levels are chosen for the surrogate model creation.

The probabilistic distribution of all the parameters is considered to be uniform between minimum/maximum bounds, specified in Table 2. The uniform distribution is chosen because of a weakly informative state of knowledge of the variability of the input parameters. Classical probability distributions are linked to well-known families of orthonormal polynomials [48]. The corresponding univariate orthogonal polynomial is of Legendre type for the uniform probability distribution.

The input sample comprising of a set of 100 different values ranging from the minimum to the maximum magnitude in uniform distribution (see Table 2) of the five most sensitive parameters are prepared for the PCE creation. UQLab provides several sampling methods based on MC and quasi MC (such as Sobol',

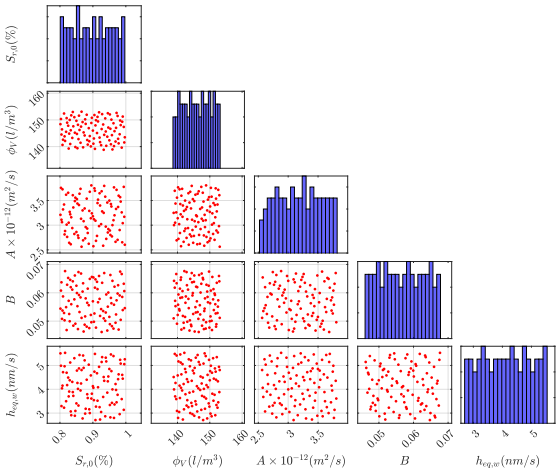

Figure 15: Input sample of size 100 (based on Sobol' sampling method) comprising of five parameters following uniform distribution in their respective ranges of variability for the creation of the polynomial chaos expansion (PCE) based surrogate model

Halton) sampling methods [49]. A Sobol' sequence sampling method is used to create the input sample, presented in Figure 15, as it provides the best parsimoniously filling the input space.

The least-angle regression (LARS) method is used to create the PCE metamodel truncated to the maximum polynomial degree of $p = 3$ using a hyperbolic truncation scheme with $q = 1$. The accuracy of the constructed PCE is estimated by computing the leave-one-out (LOO) cross-validation error (ϵ_{LOO}). This error of order 10^{-5} is reported at all three depth levels for ten validation points along with wall height for the time instance of the test VD3. Notably, PCE LOO error is of order 10^{-4} for the early pressurization tests (VPO and VC) time instances. The observation is in coherence with the stability of the

associated physical process of heating and drying. The error magnitude is in the acceptable range in the application point of view of the engineering structures [50, 51].

Additional validation of PCE metamodel accuracy is established by defining another independent sample size of 100 for its response comparison from the TH and PCE-based surrogate models. The quantitative and qualitative similarity of the degree of saturation (i.e. Y_{output}) from 100 computations on TH model (Y_{true}) and its PCE surrogate model (Y_{PC}) is presented in Figure 16. The computed PCE is very accurate with only 100 model calls. It is possibly because the study of the process is close to the boundary. Thereby, the boundary condition effect in the formulation is directly taken into account by the parameters in the boundary. Besides, the 100 model calls provide relative dominance over the decreasing boundary condition effects with increasing depth, keeping the quality of the created PCE intact for all three depths.

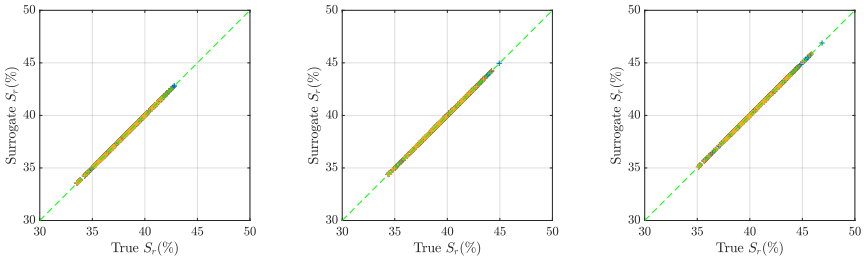

(a) at 0.5cm depth (b) at 1.5cm depth (c) at 2.5cm depth

Figure 16: Validation of the polynomial chaos expansion (PCE) based surrogate model using a Monte-Carlo (MC) simulation method based input sample of 100 size

The Sobol sensitivity indices are computed from the PCE surrogate model at

all three depth levels for the variation of the saturation ratio at the mid-height level of the wall at the instance of the pressurization test VD3. The sensitivity analysis outcome is presented in Figure 17.

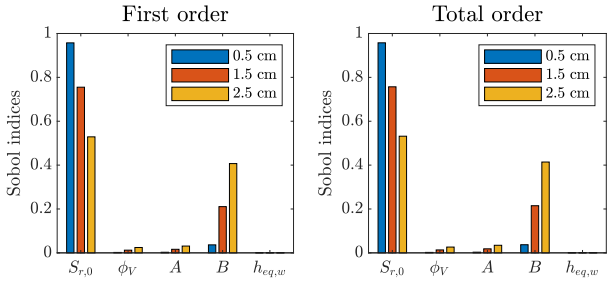

Figure 17: Sobol indices at three depth levels computed from the PCE based surrogate model (at zero cost) of the TH model at the time instance of the pressurization test VD3

The qualitative and quantitative estimations from the first order and total order Sobol' indices are close. The depth level nearest to the outer surface reflects the highest significance of the initial saturation ratio, progressively reducing towards the center of the wall. The response is in line with the observations drawn from the preliminary sensitivity analysis based on Cotter's indices (see Figure 14). Notably, the dominant effect of the initial conditions (parameter $S_{r,0}$) in comparison to the boundary conditions (parameter $h_{eq,w}$) on the model response may seem counter-intuitive. However, based on the similar trends reported from Figure 17 and Figure 14, it is observed that the boundary conditions are comparatively more influential for the early test instances (VPO and VC), while initial conditions still dominate the model response. It can be reported that the hydric boundary condition approaches to higher stability with the increasing timeline of the VeRCoRs mock-up model. Overall, almost

zero Sobol index for the $h_{eq,w}$ parameter indicates the reliability of the containment building tightness despite uncertainty and the variability in the external environmental conditions.

The available porosity remains nearly equally influential at all three depth levels while presenting a trend opposite the initial saturation ratio. The parameter B, an indirect representative of the concrete mass loss evolution, is observed to increase significantly with the increasing depth level (hence increasing the saturation ratio). It infers faster drying kinetics near the external surface resulting in comparatively quicker stability in the mass loss evolution.

The reliability in the TH model response for the saturation ratio evolution, taking into account the uncertainty in the constitutive parameters, requires many computations as per the application point of view of the law of large numbers and the central limit theorem. Therefore, many computations (of order 10^6) are carried out using the PCE metamodel to estimate the probability density function (PDF) of the degree of saturation at three different depths along with wall height. Three wall height levels *i.e.* bottom = 0 m, mid = 6.6m and top = 13.2m with an offset of 4.68m from global height coordinates of wall bottom are chosen to plot the PDF as a representative of the entire wall height response. The computed PDFs are presented in Figure 18.

The overall response at a particular depth level is qualitatively similar at all three wall height levels. Therefore, indirectly presenting the spatial homogeneity consideration of the material parameters in the TH model. At 0.5cm depth level, the PDF presents a plateau of bandwidth about 6% (between 36%

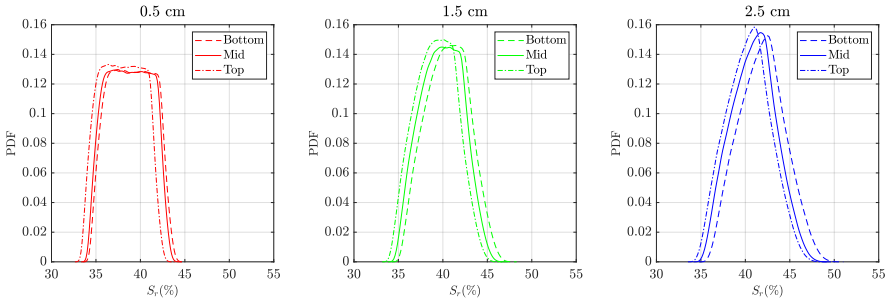

(a) (b) (c)

Figure 18: Probability density function (PDF) for the degree of saturation for the test instance of VD3 at different height and depth intervals along the wall obtained from 10^6 model computations following a Monte-Carlo (MC) simulation method

and 41%) saturation ratio. In comparison, the bandwidth of this plateau decreases with increasing depth level to about 3% at 1.5cm depth and $< 1.5\%$ at 2.5cm depth level. The decreasing trend reflects the increasing stability in the hydric exchange between the wall and outer environment with increasing depth. Also, the boundary condition effect in the TH model constitution presents the explanation of the plateau at the 0.5cm depth level. The correlation between the initial saturation ratio ($S_{r,0}$) and hydric exchange coefficient ($h_{eq,w}$) states that to obtain a similar RH, either a higher or a lower magnitude of both parameters is needed. Therefore, the varying magnitude of both parameters in 10^6 computations incorporates the effect of the boundary (via $h_{eq,w}$) to a comparatively greatest extent. The arithmetic mean of 38.71%, 39.92% and 40.98% at the mid-height wall level for 0.5cm, 1.5cm and 2.5cm depth respectively are reported from 10^6 computations based on the MC simulation method.

Further, the confidence interval of the saturation ratio magnitude is estab-

lished using the cumulative density function (CDF) of 10^6 computations, presented in Figure 19. Here, for depth level 0.5cm (see Figure 19a), the confidence interval at three height and depth levels is computed as 90% probable output by making a threshold for the zone of uncertainty (Z.U.) at the lower and upper 5% probable outcomes. The range of S_r for wall bottom and top height levels is estimated in the similar guidelines and subsequently extended to the 1.5 cm (Figure 19b) and 2.5 cm (Figure 19c) depths for the three height levels.

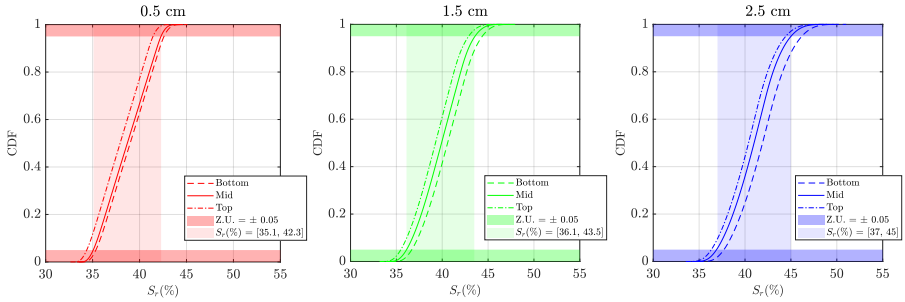

(a) (b) (c)

Figure 19: Cumulative density function (CDF) for the degree of saturation for the test instance of VD3 at different height and depth intervals along the wall obtained from 10^6 model computations following a Monte-Carlo (MC) simulation method

The blind comparison of S_r along wall height between field measurements at three depth ranges with PE, ME and M3E electrodes and numerical stochastic computations at three wall depths levels are presented in Figure 20. Here, two numerical computational parameters are presented, the arithmetic mean (μ) of 10^6 computations for ten height levels and the standard deviation (σ) in the form of the confidence interval S_r obtained from the respective CDFs. Also, the uncertainty in the capacitive measurements based saturation ratio (*i.e.* un-

certainty on the estimate of the mean value) is presented by horizontal error bars at each measurement point. The numerically estimated saturation ratios are higher than the experimental counterpart, while the experimental measurements approach the numerical estimations with increasing depth levels. The experimental measurements at all depth levels range from 0-50% as extreme limits, while most of the measurements are 20-40% range. The numerically estimated S_r presents a narrower range of about 8% in magnitude at all three depth levels with nearly similar magnitudes over the wall height with a decreasing gradient of 0.14%/m between wall bottom and top. A brief discussion on Figure 20 outcomes to establish a link between independent experimental and numerical campaigns is presented hereafter.

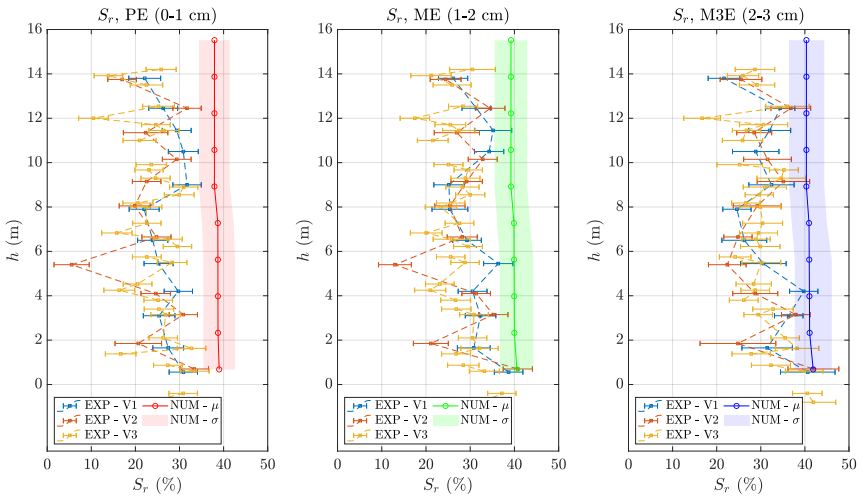

Figure 20: Comparison of experimental data exploited from three electrodes PE, ME and M3E with stochastic numerical computations at depths 0.5cm, 1.5cm and 2.5cm respectively for the saturation ratio estimations corresponding to the VD3 pressurization/depressurisation test instance

First, the uncertainty in the magnitude of the experimental porosity measurements has a direct impact on the reported saturation ratios in Figure 3. The center core porosity is reported 15.8% (average from eight cores), while the surface porosity is 14.5%. The evolution (decrease) of the porosity towards the surface suggests that the porosity on the three first centimetres could join about 13.4%. Thus, this hypothesis would increase the experimentally estimated saturation ratio by 2 to 2.5% in magnitude. Besides, the numerical mean porosity is taken as 14.6%, which is associated with the experimental porosity obtained from the surface cores. If the numerical mean porosity is changed to 15.8% (corresponding to the center core measurements), the overall stochastic TH model response decreases the S_r measurements by less than 1% in magnitude. Hence, the uncertainty in the numerical mean porosity measurements is not significant for the numerical stochastic computations. Besides, the experimental porosity measurements are sensitive to the experimental S_r computation due to their impact on the calibration curve. Increasing the surface porosity to 15.8% (from 14.5%) shall further reduce the experimental mean saturation ratio magnitude by 2.5 to 3% on average over different depth levels. Therefore, a porosity increase from 14.5% to 15.8% reduces the experimentally estimated saturation ratio magnitude by two to three times more than the numerical counterpart.

Second, the uncertainty in the magnitude of the constitutive hydric phase parameters is well identified as presented in the stochastic numerical model. However, the drying behaviour, more specifically the hydric exchange between the outer wall surface and the environment, is defined by the desorption model

presented in Equation 5. The desorption model parameters 'a' and 'b' are computed to represent the numerical desorption isotherm following the single point experimental measurement of the desorption and the concrete mass loss evolution with time at temperature of 20°C and RH of 50% [26]. Comparing the desorption isotherm database available for different concretes presents the significance of the constituent parameters 'a' and 'b'. Numerically, an increase of the two parameters by 10% decreases the numerical mean S_r to about 6.5% in magnitude at all three depth levels at the time instance of the VD3 test. Thereby, the updated desorption model shall reduce the difference between experiment and numerical saturation ratio estimations. Besides, the TH model takes into account the only reference we know for the desorption behaviour, defined at the temperature of 20°C. However, the ambient air temperatures vary between about 10°C to 35°C in the outer surface and likewise vary between about 5°C to 38°C in the inner surface (see Figure 7) over the lifetime of the VeRCoRs mock-up. In general, a lower reference temperature desorption isotherm shall lead to further higher estimations of the numerical saturation ratios and vice-versa.

Lastly, it is forbidden to extract the concrete cores from the VeRCoRs mock-up containment structure where the non-destructive measurements are performed. This restriction imposes a contradiction to the calibration recommendations [31] for the conversion of the non-destructive measurements into the degree of saturation for the VeRCoRs mock-up. In this work, the calibration procedure is carried out on concrete cores that are taken from a similar concrete mix that is poured and cured in the laboratory in different conditions than the

real structure. Therefore, the absence of a 'true' calibration curve potentially induces a global under-evaluation of the experimentally evaluated saturation ratios.

Nonetheless, for the blind comparison, the available data on the porosity measurements, desorption model and the calibration curve is used. Therefore, the results reported in Figure 20 are kept intact. Overall, the difference in the estimations from the two independent campaigns highlight the sensitivity of experimental calibration and numerical approximations on the saturation ratio estimations.

6. Conclusions

Experimental and numerical estimation of the saturation ratios in the VeRCoRs NCB structure, and their blind comparison and discussion, are presented. The in-situ capacitive measurements are carried out along three vertical lines along the outer surface of the inner wall of VeRCoRs mock-up. This NDT technique associated with three-electrode probes presented the experimental estimate of the saturation ratio on the first centimetres of the wall. A weakly coupled thermal and hydric model of an asymmetric vertical sector of VeRCoRs mock-up is presented for the deterministic and stochastic numerical estimations of the saturation ratio.

A set of eight input parameters is prepared for this study over six-time instances representative of the pressurising/depressurisation tests on VeRCoRs mock-up. Cotter's method based sensitivity analysis presented a preliminary

ranking of the influence of each parameter. The variation in the thermal phase parameters is concluded least influential in the saturation ratio estimation. The hydric phase parameters, namely initial water content ($C_{fw,0}$), free water accessible porosity (ϕ_V), diffusivity coefficients (A and B) and hydric exchange coefficient ($h_{eq,w}$) are concluded as most influential parameters for saturation ratio estimations from the TH model.

Further, the mesh design along the wall is optimised based on the consistency in the saturation ratio estimations. Finally, the knowledge of each parameter's influence and the optimised mesh design are incubated for the probabilistic analysis of the degree of saturation estimations from 3D TH model computation.

A polynomial chaos expansion (PCE) based surrogate model of the 3D TH model is created to enable a large number of computations (of order $> 10^6$), with practically zero cost, for probabilistic analysis of the saturation ratio. Comparing numerical estimations at the respective depth levels with the in-situ measurements at the latest pressurisation test instance presented consistent results. In an entirely blind approach, the minimum mean difference between the computed saturation ratio in the two approaches remains at about 6% in magnitude. However, the difference potentially reduces to 5% for the numerical computations with the mean porosity of 15.8% (instead of 14.6%). The difference further reduces to about 1% with updated desorption model parameters.

Overall, the experimental and numerical estimations are in close agreement with each other for the behaviour at the outer surface of the containment wall. Moreover, drying behaviour at the central regions of the wall is also crucial to the

durability of the containment structures. While the capacitive measurements are in the development phase for the in-situ measurements at the wall center regions, the presented TH model response can be reliably used to access the drying behaviour at the central regions. An update in the model desorption isotherm from a brand new experimental database shall increase the reliability of the TH stochastic model response. Besides, a larger input sample may be required to correctly create an accurate PCE based surrogate model of the drying behaviour at the wall center region due to its distance from the boundaries. Eventually, a complementary study could also consider the quantification and the effect of the variability of a larger number of input parameters.

Acknowledgments

The authors acknowledge the funding support from France's National Research Agency through the ENDE and MACENA projects (ProjetIA-11-RSNR-0009 and ProjetIA-11- RSNR-0012) for this work.

Appendix A. The variability considered in the in-situ measurements

Different types of variability were considered concerning on-site measurements. The first variability (Var1) is modelled linked to the repeatability of numerous measurements at the same point. The second variability (Var2) corresponds to the measurement variability in the same area assumed as homogeneous. The third variability (Var3) is the variability between different homogeneous areas of the same concrete batch. The last variability (Var4) considered is

the variability of fabrication consisting of comparing the measurements obtained on two identical concretes but fabricated in different batches and at different times.

Variance values presented in Table A.3 correspond to averages from six concrete mixes having the same components (rolled siliceous aggregates, granulometry, cement CEM I 52.5 NCalcia) but different water/cement ratios from 0.31 to 0.9, inducing different porosities. During this ANR-SENSO project [8], only electrodes PE and ME were tested, M3E being designed several years later.

Table A.3: Variances of permittivity (-) related to capacitive electrodes measured in the project ANR-SENSO

Electrode	Variance	Saturated state	Dry state
ine	Var1	9.43×10^{-4}	8.33×10^{-6}
ME	Var2	4.10×10^{-3}	1.68×10^{-5}
	Var3	2.67×10^{-1}	1.08×10^{-1}
	Var4	3.54	3.23×10^{-1}
ine	Var1	2.11×10^{-2}	1.16×10^{-4}
PE	Var2	3.20×10^{-2}	8.90×10^{-5}
	Var3	1.47	8.91×10^{-2}
	Var4	2.18	2.41×10^{-1}

The order of difference between variances related to punctual measurements (Var1 and Var2) and those corresponding to regional or global measurements (Var3 and Var4) can be seen. This is because these data are obtained in sim-

ilar indoor conditions. Thus, the variance is only due to the concrete and the electronics of the capacitive sensor variabilities. Furthermore, the variability increase for saturated concretes can be interpreted as porosity variations.

Appendix B. Theory of the implemented stochastic methods

Appendix B.1. Cotter's sensitivity analysis method

Consider the input vector of the set of eight TH model parameters as $\boldsymbol{x} = \{x_1, ..., x_8\}^T \in \mathcal{D}_x$. Each input variable, X_i, is varied between its minimum, x_i^-, and maximum, x_i^+, magnitudes following a systematic sequence of model evaluations with N = 8 input variables as listed hereafter. So, for an equivalent mathematical model $\mathcal{M}(X)$ of the TH FE model, Cotter's method is implemented as follows:

- One run with all variables at their minimum values: $S_r^1 = \mathcal{M}(x_1^-, ..., x_8^-)$
- Eight runs at minimum magnitude, switching one variable at a time to its maximum magnitude: $S_r^{i+1} = \mathcal{M}(x_1^-, ..., x_i^+, ..., x_8^-), i = 1, ..., 8$
- Eight runs at maximum magnitude, switching one variable at a time to its minimum magnitude: $S_r^{i+9} = \mathcal{M}(x_1^+, ..., x_i^-, ..., x_8^+), i = 1, ..., 8$
- One run with all variables at their maximum values: $S_r^{18} = \mathcal{M}(x_1^+, ..., x_8^+)$

Here, $\boldsymbol{x} = \{x_1, ..., x_8\}^T = \{\lambda_{hc}, h_{eq,th}, C_{fw,0}, \phi_V, A, B, h_{eq,w}, E_a^w\}^T$ is the input variable vector.

The computed saturation ratio (S_r) from 18 model evaluations is processed at each input variable X_i, where $i \in [1, 8]$ for the expectation of the importance

of the odd and even order effects. Equation B.1 presents the formulation of the odd ($C_o(i)$) and even ($C_e(i)$) order effects expectation for each input variable.

$$\begin{aligned} C_o(i) &= \frac{1}{4}\left[(S_r^{18} - S_r^{i+9}) + (S_r^{i+1} - S_r^1)\right] \\ C_e(i) &= \frac{1}{4}\left[(S_r^{18} - S_r^{i+9}) - (S_r^{i+1} - S_r^1)\right] \end{aligned} \tag{B.1}$$

Subsequently, the importance of each variable is measured by the Cotter index (I_{Cotter}):

$$I_{Cotter}(i) =\mid C_o(i) \mid + \mid C_e(i) \mid \tag{B.2}$$

Appendix B.2. PCE surrogate model

Consider TH model represented by a $\mathcal{M}(\mathbf{X})$ as an equivalent mathematical model. Here, $\mathbf{X} \in \mathbb{R}^M$ is a random vector with independent components described by the joint probability density function (PDF) $f_{\mathbf{X}}$. Consider also a finite variance computational model as a map $Y = \mathcal{M}(\mathbf{X})$, with $Y \in \mathbb{R}$ such that:

$$\mathbb{E}\left[Y^2\right] = \int_{\mathcal{D}_{\mathbf{X}}} \mathcal{M}(\boldsymbol{x})^2 f_{\mathbf{X}}(\boldsymbol{x}) \mathrm{d}\boldsymbol{x} < \infty \tag{B.3}$$

Then, under the assumption of Equation B.3, the PCE of $\mathcal{M}(\mathbf{X})$ is defined as:

$$Y = \mathcal{M}(\mathbf{X}) = \sum_{\boldsymbol{\alpha} \in \mathbb{N}^M} y_{\boldsymbol{\alpha}} \Psi_{\boldsymbol{\alpha}}(\mathbf{X}) \tag{B.4}$$

where, the $\Psi_{\boldsymbol{\alpha}}(\mathbf{X})$ are multivariate polynomials orthonormal with respect to $f_{\mathbf{X}}$, $\alpha \in \mathbb{N}^M$ is a multi-index that identifies the components of the multivariate polynomials $\Psi_{\boldsymbol{\alpha}}$ and the $y_\alpha \in \mathbb{R}$ are the corresponding coefficients. In practical applications, the sum in Equation B.4 needs to be truncated to a finite sum by introducing the truncated polynomial chaos expansion:

$$\mathcal{M}(\mathbf{X}) \approx \mathcal{M}^{PC}(\mathbf{X}) = \sum_{\boldsymbol{\alpha} \in \mathcal{A}} y_{\boldsymbol{\alpha}} \Psi_{\boldsymbol{\alpha}}(\mathbf{X}) \tag{B.5}$$

where, $\mathcal{A} \subset \mathbb{N}^M$ is the set of selected multi-indices of multivariate polynomials.

In this work, the least-angle regression (LARS) method is used to create the PCE metamodel truncated to the maximum polynomial degree of $p = 3$ using hyperbolic truncation scheme with $q = 1$.

$$\mathcal{A}^{M,p,q} = \{\boldsymbol{\alpha} \in \mathcal{A}^{M,p} \ : \ \|\boldsymbol{\alpha}\|_q \leq p\}, \ where \ , \|\boldsymbol{\alpha}\|_q = \left(\sum_{i=1}^{M} \alpha_i^q \right)^{1/q} \tag{B.6}$$

The accuracy of the constructed PCE is estimated by computing the leave-one-out (LOO) cross-validation error (ϵ_{LOO}). It consists in building N meta-models $\mathcal{M}^{PC\setminus i}$, each one created on a reduced experimental design $\mathfrak{X}\setminus\mathbf{x}^{(i)} = \mathbf{x}^{\{}(j), j = 1, ..., N, j \neq i\}$ and comparing its prediction on the excluded point $\mathbf{x}^{(i)}$ with the real value $y^{(i)}$.). The leave-one-cross-validation error can be writ-

ten as:

$$\epsilon_{LOO} = \frac{\sum_{i=1}^{N} \left(\mathcal{M}(\mathbf{x}^{(i)} - \mathcal{M}^{PC\setminus i}(\mathbf{x}^{(i)}) \right)^2}{\sum_{i=1}^{N} \left(\mathcal{M}(\mathbf{x}^{(i)} - \hat{\mu}_Y \right)^2} \tag{B.7}$$

where, $\hat{\mu}_Y$ is the mean of the experimental design sample.

References

[1] M. Corbin, M. Garcia, Benchmark vercors report 2015, 2015. URL: https://www.edf.fr/edf/accueil-magazine/une-maquette-de-30-metres-de-haut-pour-la-recherche.

[2] D. Aggelis, T. Shiotani, Repair evaluation of concrete cracks using surface and through-transmission wave measurements, Cement and Concrete Composites 29 (2007) 700–711.

[3] O. Abraham, B. Piwakowski, G. Villain, O. Durand, Non-contact, automated surface wave measurements for the mechanical characterisation of concrete, Construction and Building Materials 37 (2012) 904–915. Non Destructive Techniques for Assessment of Concrete.

[4] S. Laurens, J. Balayssac, J. Rhazi, G. Klysz, G. Arliguie, Non-destructive evaluation of concrete moisture by gpr: experimental study and direct modeling, Materials and structures 38 (2005) 827–832.

[5] X. Dérobert, J.-P. Balayssac, Z. M. Sbartaï, J. Dumoulin, 3 - electromagnetic methods, in: J.-P. Balayssac, V. Garnier

(Eds.), Non-Destructive Testing and Evaluation of Civil Engineering Structures, Elsevier, 2018, pp. 87–137. URL: https://www.sciencedirect.com/science/article/pii/B9781785482298500030. doi:https://doi.org/10.1016/B978-1-78548-229-8.50003-0.

[6] X. Dérobert, J. Iaquinta, G. Klysz, J.-P. Balayssac, Use of capacitive and gpr techniques for the non-destructive evaluation of cover concrete, NDT & E International 41 (2008) 44–52.

[7] X. Dérobert, J. Lataste, J.-P. Balayssac, S. Laurens, Evaluation of chloride contamination in concrete using electromagnetic non-destructive testing methods, NDT & E International 89 (2017) 19–29.

[8] J. Balayssac, S. Laurens, G. Arliguie, D. Breysse, V. Garnier, X. Derobert, B. Piwakowski, Description of the general outlines of the french project SENSO - Quality assessment and limits of different NDT methods, Construction and Building Materials 35 (2012) 131–138.

[9] D.-M. Bouhjiti, M. Boucher, M. Briffaut, F. Dufour, J. Baroth, B. Masson, Accounting for realistic thermo-hydro-mechanical boundary conditions whilst modeling the ageing of concrete in nuclear containment buildings: Model validation and sensitivity analysis, Engineering Structures 166 (2018) 314 – 338.

[10] J. B. J. Fourier, Théorie analytique de la chaleur, Mem. Acad. R. Sci 8 (1829) 581–622.

[11] R. Mensi, P. Acker, A. Attolou, Séchage du béton: analyse et modélisation, Materials and structures 21 (1988) 3–12.

[12] Z. P. Bažant, V. Křístek, J. L. Vitek, Drying and cracking effects in box-girder bridge segment, Journal of Structural Engineering 118 (1992) 305–321.

[13] Z. Bažant, L. Najjar, Nonlinear water diffusion in nonsaturated concrete, Matériaux et Construction 5 (1972) 3–20.

[14] L. Granger, Comportement différé du béton dans les enceintes de centrales nucléaires: analyse et modélisation, Ph.D. thesis, 1995.

[15] O. Coussy, R. Eymard, T. Lassabatère, Constitutive modeling of unsaturated drying deformable materials, Journal of Engineering Mechanics 124 (1998) 658–667.

[16] A. Sellier, S. Multon, L. Buffo-Lacarrière, T. Vidal, X. Bourbon, G. Camps, Concrete creep modelling for structural applications: non-linearity, multi-axiality, hydration, temperature and drying effects, Cement and Concrete Research 79 (2016) 301–315.

[17] M. Sánchez, B. Pomaro, A. Gens, Coupled thm analysis of a full-scale test for high-level nuclear waste and spent fuel disposal under actual repository conditions during 18 years of operation, Géotechnique 0 (0) 1–43.

[18] P. Baggio, C. E. Majorana, B. A. Schrefler, Thermo-hygro-mechanical

analysis of concrete, International Journal for Numerical Methods in Fluids 20 (1995) 573–595.

[19] V. A. Salomoni, C. E. Majorana, B. Pomaro, G. Xotta, F. Gramegna, Macroscale and mesoscale analysis of concrete as a multiphase material for biological shields against nuclear radiation, International Journal for Numerical and Analytical Methods in Geomechanics 38 (2014) 518–535.

[20] Le Pape, Y and Benboudjema, F and Meftah, F, Numerical analysis of the delayed behavior of french NNP double containments, in: VIII International Conference on Computational Plasticity, 2003.

[21] M. Asali, B. Capra, J. Mazars, J.-B. Colliat, Numerical strategy for forecasting the leakage rate of inner containments in double-wall nuclear reactor buildings, Journal of Advanced Concrete Technology 14 (2016) 408–420.

[22] D. Rossat, D. E.-M. Bouhjiti, J. Baroth, M. Briffaut, F. Dufour, A. Monteil, B. Masson, S. Michel-Ponnelle, A bayesian strategy for forecasting the leakage rate of concrete containment buildings – application to nuclear containment buildings, Nuclear Engineering and Design 378 (2021) 111184.

[23] J. Niepceron, Invitation to participate in edf - vercors 3rd benchmark, 2020. URL: https://www.rilem.net/news/invitation-to-participate-in-edf-vercors-3rd-benchmark-405.

[24] M. Asali, Modélisation et prévision du comportement thermo-hydro-mécanique d'une paroi en béton : application au cas des enceintes de

confinement des bâtiments réacteurs nucléaires, Ph.D. thesis, 2016. URL: http://www.theses.fr/2016LIL10143, thèse de doctorat dirigée par Colliat, Jean-BaptisteMazars, Jacky et Capra, Bruno Génie civil Lille 1 2016.

[25] J.-L. Costaz, Confinement. Enceintes, Ed. Techniques Ingénieur, 1997.

[26] D. M. E. Bouhjiti, Analyse probabiliste de la fissuration et du confinement des grands ouvrages en béton armé et précontraint, Ph.D. thesis, Université Grenoble Alpes, 2018.

[27] G. Villain, A. Ihamouten, X. Dérobert, Determination of concrete water content by coupling electromagnetic methods: Coaxial/cylindrical transition line with capacitive probes, NDT & E International 88 (2017) 59–70.

[28] M. Adous, P. Quéffélec, L. Laguerre, Coaxial/cylindrical transition line for broadband permittivity measurement of civil engineering materials, Measurement Science and Technology 17 (2006) 2241–2246.

[29] X. Dérobert, G. Villain, Development of a multi-linear quadratic experimental design for the em characterization of concretes in the radar frequency-band, Construction and Building Materials 136 (2017) 237–245.

[30] X. Dérobert, G. Villain, Effect of water and chloride contents and carbonation on the electromagnetic characterization of concretes on the gpr frequency band through designs of experiment, NDT & E International 92 (2017) 187–198.

[31] G. Villain, V. Garnier, Z. M. Sbartaï, X. Derobert, J.-P. Balayssac, Devel-

opment of a calibration methodology to improve the on-site non-destructive evaluation of concrete durability indicators, Materials and Structures 51 (2018) 1–14.

[32] AFGC, Grandubé - grandeurs associées à la durabilité des bétons, 2007. URL: https://www.afgc.asso.fr/publication/grandube-grandeurs-associees-a-la-durabilite-des-betons/.

[33] M. Fares, Y. Fargier, G. Villain, X. Derobert, S. P. Lopes, Determining the permittivity profile inside reinforced concrete using capacitive probes, NDT & E International 79 (2016) 150–161.

[34] S. Chataigner, J.-L. Saussol, X. Dérobert, G. Villain, C. Aubagnac, Temperature influence on electromagnetic measurements of concrete moisture, European Journal of Environmental and Civil Engineering 19 (2015) 482–495.

[35] M. M. Jensen, B. Johannesson, M. R. Geiker, A numerical comparison of ionic multi-species diffusion with and without sorption hysteresis for cement-based materials, Transport in Porous Media 107 (2015) 27–47.

[36] B. Johannesson, Prestudy on diffusion and transient condensation of water vapor in cement mortar, Cement and Concrete Research 32 (2002) 955–962.

[37] R. Witasse, Contribution à la compréhension du comportement d'une coque d'aéroréfrigérant vieilli, Ph.D. thesis, 2000. URL: http://www.theses.fr/2000ISAL0096, thèse de doctorat dirigée par Reynouard, Jean-Marie Génie civil Lyon, INSA 2000.

[38] M. Thiery, V. Baroghel-Bouny, N. Bourneton, G. vilain, C. Stéfani, Modélisation du séchage des bétons. analyse des différents modes de transfert hydrique, Revue européenne de génie civil 11 (2007).

[39] P. Sémété, B. Février, Y. L. Pape, J. Delorme, J. Sanahuja, A. Legrix, Concrete desorption isotherms and permeability determination: effects of the sample geometry, European Journal of Environmental and Civil Engineering 21 (2017) 42–62.

[40] Electricité de France, Code Aster: Finite element Analysis of Structures and Thermomechanics for Studies and Research, 1989-2021. URL: www.code-aster.org.

[41] M. Briffaut, Etude de la fissuration au jeune âge des structures massives en béton : influence de la vitesse de refroidissement, des reprises de bétonnage et des armatures, Ph.D. thesis, 2010. URL: http://www.theses.fr/2010DENS0030.

[42] T. Powers, T. Brownyard, Physical properties of hardened portland cement paste: Iii, Proc. Amer. Concr. Inst. 43 (1946) 469–504.

[43] I. M. Sobol, A screening design for factorial experiments with interactions, Mathematical and Computer Modelling 1 (1993) 407–414.

[44] S. Marelli, C. Lamas, B. Sudret, UQLab user manual - sensitivity analysis, 2015. doi:10.13140/RG.2.1.1419.4404.

[45] S. C. Cotter, A screening design for factorial experiments with interactions, Biometrika 66 (1979) 317–320.

[46] M. D. Morris, Factorial sampling plans for preliminary computational experiments, Technometrics 33 (1991) 161–174.

[47] S. Marelli, B. Sudret, Uqlab user manual - polynomial chaos expansions, 2015. doi:10.13140/RG.2.1.3778.7366.

[48] D. Xiu, G. E. Karniadakis, The Wiener-Askey Polynomial Chaos for Stochastic Differential Equations, SIAM Journal on Scientific Computing 24 (2002) 619–644.

[49] H. Niederreiter, 1. Monte Carlo Methods and Quasi-Monte Carlo Methods, 1992, pp. 1–12. URL: https://epubs.siam.org/doi/abs/10.1137/1.9781611970081.ch1. doi:10.1137/1.9781611970081.ch1. arXiv:https://epubs.siam.org/doi/pdf/10.1137/1.9781611970081.ch1.

[50] M. A. Hariri-Ardebili, B. Sudret, Polynomial chaos expansion for uncertainty quantification of dam engineering problems, Engineering Structures 203 (2020) 109631.

[51] X. Guo, D. Dias, C. Carvajal, L. Peyras, P. Breul, Reliability analysis of embankment dam sliding stability using the sparse polynomial chaos expansion, Engineering Structures 174 (2018) 295 – 307.